

14.1 Introduction

Biofluid dynamics encompasses the topics of fluid flow, fluid–structure interaction, and heat and mass transfer in mammalian systems and in medical devices. Unlike standard engineering applications, understanding human body biofluid dynamics is extremely complex. This is due to the fact that *in vivo* experiments are not easy to perform and *in vitro* experiments may not always reflect the reality. Noninvasive experiments on humans are useful but do not always give the desired result. Thus, both theoretical and computational biofluid dynamics play a major role in the understanding of human body biofluid dynamics. The extracorporeal systems, such as blood pumps, can be experimentally tested. However, computational fluid dynamics is very useful at the early stages of design and development. The topics covered in this chapter are divided into one-dimensional systemic circulation and multidimensional subject-specific studies. These two topics are selected as they are realistic and provide useful information to understand diseases. Flow in model geometry and extracorporeal systems needs no special fluid dynamics treatment and thus the techniques discussed in the previous chapters may directly be applied to such problems.

14.2 Flow in human arterial system

A one-dimensional flow model is a useful tool for gaining a better understanding of blood flow in a systemic circulation¹ and how it is influenced by various interventions or diseases. At present, 3D modeling of the entire human arterial tree is not feasible within a reasonable amount of time. Apart from the unavailability of precise information regarding 3D geometry and material properties, the computational time required to model such an extensive network of branching vessels, including the fluid–structure interaction between blood and vessel walls, is simply too great. It has long been recognized that the wavelengths of the pressure-flow waves produced by the heart are much greater than the diameter of the vessels, thus it is valid to consider flow in the arteries to be quasi-one-dimensional [1–4]. The one-dimensional equations of flow are expressed in terms of vessel cross-sectional area A , velocity u , and

¹Systemic circulation consists of all arteries and veins.

pressure p as discussed in the previous chapter. Pressure is related to A via the chosen nonlinear elastic wall law (i.e., $p = p(A)$). There are indeed several to choose from (for example, see Ref. [5]) which reflects the fact that the wall law is an empirical and/or mathematical simplification of the true mechanics of vessel walls, which are anisotropic and not perfectly cylindrical. It is also well known [6–8] that the arterial wall is a viscoelastic material and thus pressure is determined not only by A but its time derivatives also, although usually these effects are generally considered small enough to be ignored [9]. Another consideration is the treatment of blood viscosity. While various approximations have been used [3,4,10], most authors [9,11–13] calculate its effects in 1D by using an assumption of fully developed Newtonian steady flow with a parabolic velocity profile over a given cross-section (Poiseuille flow).

A typical human arterial network is shown in Fig. 14.1. Table 14.1 presents details on the majority of physical artery models available in the literature. The starting point of the physical model usually is the left ventricle.² A base pressure signal of two fused sigmoid functions is the input into the ventricle. The aortic valve then (see Fig. 14.1b) regulates and directs the flow into the aorta. The pulsatile flow is then naturally allowed to pass through the arteries until the location where the network is truncated to obtain a manageable flow network. At the point of truncation, appropriate resistance should be included to represent the microcirculation.

Although a one-dimensional fluid–structure interaction model has been presented in the previous chapter, there are some additional issues that need to be addressed before the flow in the systemic arterial circulation can be fully studied. The additional information required includes representation of the left ventricle, aortic valve, bifurcations, and boundary conditions at the truncation points.

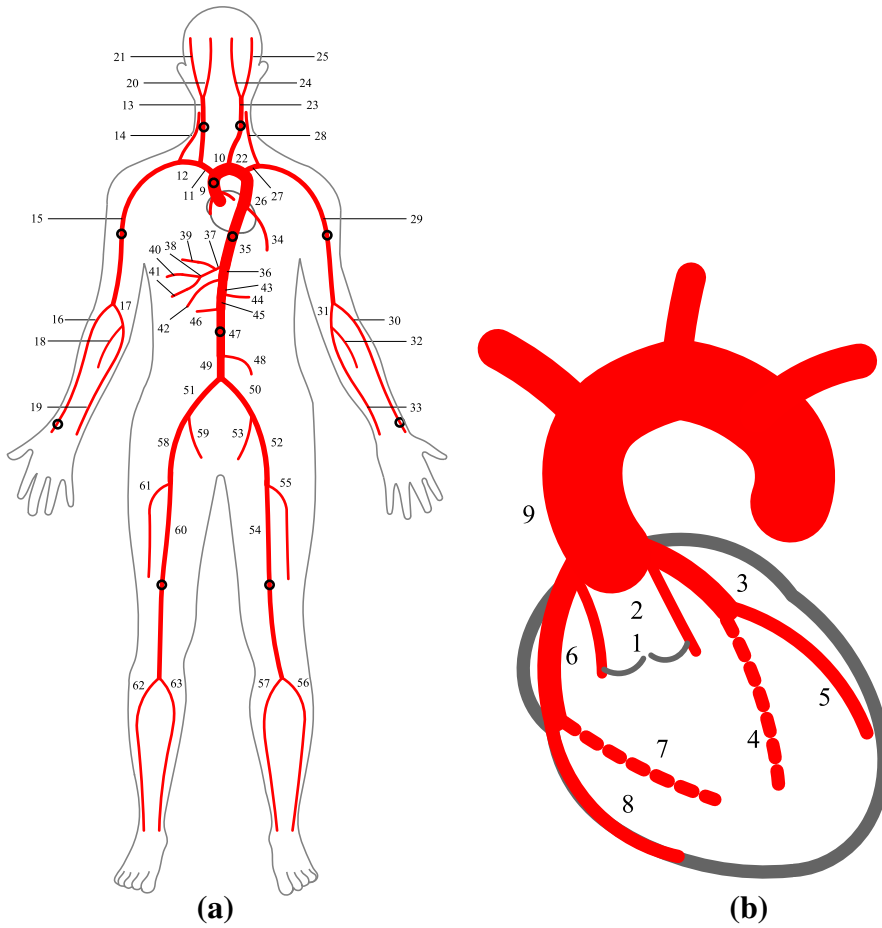
14.2.1 Heart

The heart model requires an appropriate representation of left ventricular pressure, aortic valve and coronary arteries. All arteries usually are modeled as circular cross-sectional tubes with flexible walls.

14.2.1.1 Ventricle

In the ventricle, a normal heart cycle consists of four phases: (1) In the *isovolumic contraction phase*, the ventricle begins to contract but the valve is closed. During this time there is a rapid increase in ventricular pressure since the ventricle is a closed cavity. (2) The *ejection phase* begins when ventricular pressure rises above aortic pressure, causing the valve to open. Further contraction causes ventricular pressure to rise above aortic pressure resulting in flow output, but this pressure difference is relatively small since (under normal conditions) there is little resistance to flow. (3) In the *isovolumic relaxation phase*, the heart muscle relaxes causing a drop in pressure and flow in both the ventricle and aorta. When aortic flow reaches zero, the valve closes, but there is often a small amount of reverse aortic flow before the valve is fully

²Left part of the heart from where oxygenated blood is pumped into the aorta.

**FIGURE 14.1**

(a) A typical human systemic arterial circulation network. (b) Representation of the heart within a one-dimensional framework.

closed. After the valve closes, ventricular pressure continues to fall rapidly to near zero pressure. (4) The final phase is *diastolic filling*, where the heart muscle is relaxed and, similar to a compliant balloon, increases in volume but with little increase in pressure. All these four stages can be mathematically represented using pressure variations.

As mentioned previously, the heart (left ventricle) is the input to the network model. A realistic pressure waveform within the ventricle may be generated using two sigmoid functions fused at mid-ejection (see Fig. 14.2). Each sigmoid has the form

$$p_{sig}(t) = a_1 + \frac{(a_2 - a_1)}{1 + e^{(a_3 - t)/a_4}} \quad (14.1)$$

Table 14.1 Major Arteries Used in the Present Study. The ID Numbers and Name Correspond to Those in Figure 14.1.

ID	Vessel	L (cm)	r_0 (cm)	r_0 Taper	h (cm)	$E \times 10^6$	E Taper
						(dyne/cm ²)	
1	LV Outflow Tract	1.0	1.494	—	0.168	4.0	—
2	Aortic Root	1.0 ^a	1.494 ^a	—	0.168 ^a	4.0 ^a	—
3	Left Coronary Artery	3.0 ^a	0.259 ^a	—	0.080 ^a	8.0 ^a	—
4	Left Subendocardial	7.0 ^a	0.195 ^a	−0.293	0.080 ^a	8.0 ^a	—
5	Left Subepicardial	7.0 ^a	0.195 ^a	−0.293	0.080 ^a	8.0 ^a	—
6	Right Coronary Artery	3.0 ^a	0.239 ^a	—	0.080 ^a	8.0 ^a	—
7	Right Subendocardial	7.0 ^a	0.181 ^a	−0.293	0.080 ^a	8.0 ^a	—
8	Right Subepicardial	7.0 ^a	0.181 ^a	−0.293	0.080 ^a	8.0 ^a	—
9	Ascending Aorta	4.0 ^a	1.470 ^a	−0.020	0.163 ^d	4.0 ^a	—
10	Aortic Arch I	2.0 ^a	1.120 ^a	—	0.126 ^d	4.0 ^a	—
11	Brachiocephalic	3.5 ^c	0.650 ^c	−0.046	0.080 ^d	4.5 ^c	—
12	Right Subclavian I	3.5 ^c	0.425 ^c	−0.042	0.067 ^d	3.0 ^c	—
13	Right Carotid	9.4 ^b	0.675 ^b	−0.481	0.063 ^d	7.5 ^b	−0.467
14	Right Vertebral	13.5 ^c	0.200 ^c	—	0.045 ^d	6.5 ^c	—
15	Right Subclavian II	39.8 ^c	0.407 ^c	−0.435	0.067 ^d	3.0 ^c	−0.333
16	Right Radial	22.0 ^c	0.175 ^c	−0.200	0.043 ^d	6.5 ^c	−0.154
17	Right Ulnar I	6.7 ^c	0.215 ^c	—	0.046 ^d	6.0 ^c	—
18	Right Interosseous	7.0 ^c	0.100 ^c	—	0.028 ^d	14.0 ^c	—
19	Right Ulnar II	17.0 ^c	0.203 ^c	−0.113	0.046 ^d	11.0 ^c	−0.091
20	Right Internal Carotid	17.8 ^b	0.285 ^b	−0.246	0.045 ^d	6.5 ^b	−0.231
21	Right External Carotid	10.2 ^b	0.250 ^b	−0.300	0.042 ^d	6.5 ^b	−0.231
22	Aortic Arch II	3.9 ^a	1.070 ^a	—	0.115 ^d	4.0 ^a	—
23	Left Carotid	13.9 ^b	0.600 ^b	−0.500	0.063 ^d	7.0 ^b	−0.500
24	Left Internal Carotid	17.8 ^b	0.265 ^b	−0.226	0.045 ^d	6.5 ^b	−0.231
25	Left External Carotid	10.2 ^b	0.235 ^b	−0.255	0.042 ^d	6.5 ^b	−0.231
26	Thoracic Aorta I	5.2 ^a	0.999 ^a	—	0.110 ^d	4.0 ^a	—
27	Left Subclavian I	3.5 ^c	0.425 ^c	−0.042	0.066 ^d	3.0 ^c	—
28	Left Vertebral	13.5 ^c	0.200 ^c	—	0.045 ^d	6.5 ^c	—
29	Left Subclavian II	39.8 ^c	0.407 ^c	−0.435	0.067 ^d	3.0 ^c	−0.333
30	Left Radial	22.0 ^c	0.175 ^c	−0.200	0.043 ^d	6.5 ^c	−0.154
31	Left Ulnar I	6.7 ^c	0.215 ^c	—	0.046 ^d	6.0 ^c	—
32	Left Interosseous	7.9 ^c	0.100 ^c	—	0.028 ^d	14.0 ^c	—
33	Left Ulnar II	17.0 ^c	0.203 ^c	−0.113	0.046 ^d	11.0 ^c	−0.091
34	Intercostals	8.0 ^a	0.620 ^a	−0.250	0.049 ^d	4.0 ^a	−0.250
35	Thoracic Aorta II	10.4 ^a	0.675 ^a	−0.044	0.100 ^d	4.0 ^a	—
36	Abdominal Aorta I	5.3 ^a	0.610 ^a	—	0.090 ^d	4.0 ^a	—
37	Celiac I	1.0 ^a	0.390 ^a	−0.487	0.064 ^d	4.0 ^a	—
38	Celiac II	1.0 ^a	0.200 ^a	—	0.064 ^d	4.0 ^a	—
39	Hepatic	6.6 ^a	0.220 ^a	—	0.049 ^d	4.0 ^a	—
40	Gastric	6.3 ^a	0.180 ^a	—	0.045 ^d	4.0 ^a	—
41	Splenic	7.1 ^a	0.275 ^a	—	0.054 ^d	4.0 ^a	—
42	Superior Mesenteric	5.9 ^a	0.300 ^a	—	0.069 ^d	4.0 ^a	—
43	Abdominal Aorta II	1.0 ^a	0.590 ^a	—	0.080 ^d	4.0 ^a	—

(continued)

Table 14.1 (Continued)

ID	Vessel	L (cm)	r_0 (cm)	r_0 Taper	h (cm)	$E \times 10^6$ (dyne/cm ²)	E Taper
44	Left Renal	3.2 ^a	0.260 ^a	—	0.053 ^d	4.0 ^a	—
45	Abdominal Aorta III	1.0 ^a	0.590 ^a	—	0.080 ^d	4.0 ^a	—
46	Right Renal	3.2 ^a	0.260 ^a	—	0.053 ^d	4.0 ^a	—
47	Abdominal Aorta IV	10.6 ^a	0.580 ^a	−0.055	0.075 ^d	4.0 ^a	—
48	Inferior Mesenteric	5.0 ^a	0.160 ^a	—	0.043 ^d	4.0 ^a	—
49	Abdominal Aorta V	1.0 ^a	0.520 ^a	—	0.065 ^d	4.0 ^a	—
50	Left Common Iliac	5.8 ^a	0.400 ^c	−0.075	0.060 ^d	4.0 ^a	—
51	Right Common Iliac	5.9 ^a	0.400 ^c	−0.075	0.060 ^d	4.0 ^a	—
52	Left External Iliac	14.4 ^a	0.370 ^c	−0.152	0.053 ^d	8.0 ^a	—
53	Left Internal Iliac	5.0 ^a	0.200 ^c	—	0.040 ^d	16.0 ^a	—
54	Left Femoral	44.3 ^a	0.314 ^c	−0.124	0.050 ^d	8.0 ^a	—
55	Left Deep Femoral	12.6 ^a	0.200 ^c	—	0.047 ^d	8.0 ^a	1.000
56	Left Posterior Tibial	32.1 ^a	0.175 ^c	—	0.045 ^d	16.0 ^a	—
57	Left Anterior Tibial	34.3 ^a	0.275 ^c	−0.091	0.039 ^d	16.0 ^a	—
58	Right External Iliac	14.5 ^a	0.370 ^c	−0.152	0.053 ^d	8.0 ^a	—
59	Right Internal Iliac	5.0 ^a	0.200 ^c	—	0.040 ^d	16.0 ^a	—
60	Right Femoral	44.4 ^a	0.314 ^c	−0.124	0.050 ^d	8.0 ^a	—
61	Right Deep Femoral	12.7 ^a	0.200 ^c	—	0.047 ^d	8.0 ^a	1.000
62	Right Posterior Tibial	32.2 ^a	0.175 ^c	—	0.045 ^d	16.0 ^a	—
63	Right Anterior Tibial	34.4 ^a	0.275 ^c	−0.091	0.039 ^d	16.0 ^a	—

Vessel Length (L) and Wall Thickness (h), Proximal Radius (r_0), and Young's Modulus (E), Both with the Degree of Linear Tapering Shown in Fractional Decrease (Negative Values) or Increase (Positive Values).^{a–d}

^a Mynard and Nithiarasu [14].

^b Reymond et al. [15].

^c Liang et al. [16, 17].

^d Wang and Parker [18].

where

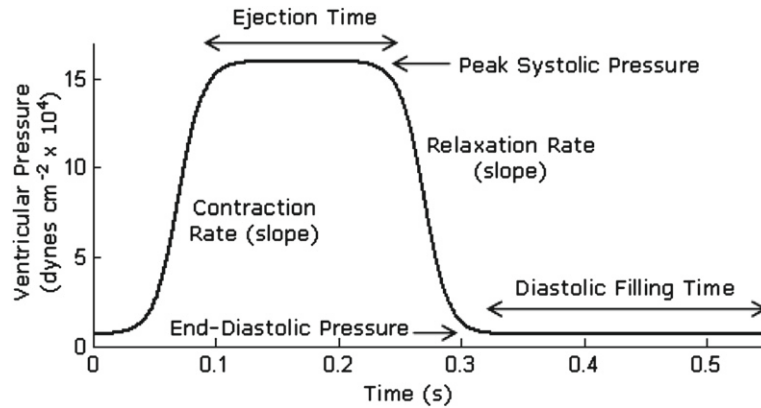
$$a_1 = p_{ed} - 9.11 \times 10^{-4} p_{peak}$$

$$a_2 = p_{peak}$$

$$a_3 = 7t_c$$

$$a_4 = t_c$$

Here, p_{ed} is end-diastolic pressure, p_{peak} is peak pressure, and t_c is a time constant that determines the slope of the isovolumic upstroke or downstroke. From end-diastole to peak pressure (i.e., the first sigmoid) Eq. (14.1) is used as is, but from peak pressure onwards (the second sigmoid) the relation is calculated backwards in time and applied forwards in time. Where the two sigmoids join (peak pressure), an iterative technique is used to ensure the pressures of the adjacent points are similar to within a threshold. This avoids a jump in pressure that would occur when fusing two sigmoids that

**FIGURE 14.2**

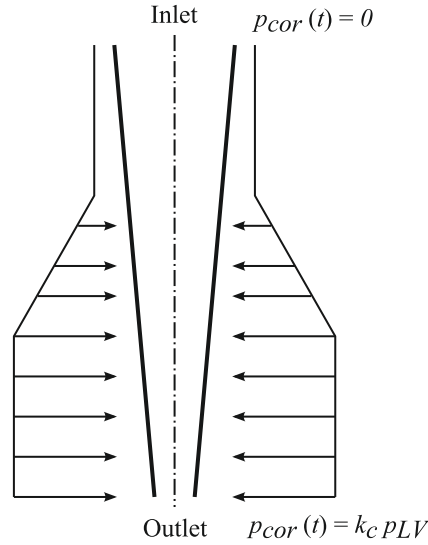
An example of a realistic ventricular pressure constructed using two sigmoid functions and used (in combination with a valve model) as the input to the arterial model. Important physiological features are labeled.

have different shapes (for example, when using a different value of t_c for isovolumic contraction and relaxation). The benefit of this input is that important features of real ventricular pressures can be emulated and manipulated independently. These features are end-diastolic pressure, peak pressure, ejection time, contraction rate, relaxation rate, and diastolic filling time as shown in Fig. 14.2, as well as heart rate, which results from a combination of the other parameters.

14.2.1.2 Coronary flow

Coronary arteries supply blood to the heart muscle. There are two inlets to the coronary circulation (the left and right coronary arteries, LCA and RCA, respectively) and these are located behind two of the three cusps of the aortic valve. It is well known [19] that the majority of coronary flow to the LV occurs during diastole when the valve is closed. This is because during systole, the contracting muscle compresses the subendocardial coronary arterioles and capillaries, which reduces or even reverses total left coronary flow. However, during diastole the heart muscle is relaxed and there is no restriction to flow.

The situation is somewhat different in the right coronary artery which feeds the RV. Since the pressure generated by the RV is lower than the LV, there is less compression of the subendocardial coronary vessels and thus greater systolic flow. Similar to Wang and Parker [20], the effect of coronary flow on arterial flow can be approximated by assuming there is no coronary flow during systole, and by making $R_{VR} < 1$ when the valve is fully closed (see below). It is also possible to model regional coronary flow explicitly [14], with LCA and RCA both branching into two “equivalent” vessels that represent the lumped behavior of the left and right coronary arterial circulations, respectively. Each of these equivalent vessels have a linear taper in A_0 . This is a

**FIGURE 14.3**

Representation of external pressure distribution on the coronary artery induced by the heart.

similar approach to that taken by Rumberger [21], who used an equivalent vessel with an elastic taper (i.e., taper of β rather than A_0) to represent the coronary circulation. Thus in the current model, blood flows from the ventricle (input) into the aortic root, where a trifurcation is formed from the two coronary equivalent vessels and ascending aorta (see Fig. 14.1b). Furthermore, and similar to Guiot et al. [22], the effect of the surrounding heart muscle on the subendocardial vessels is simulated by applying a time-varying external pressure $p_{ext}(t)$ to the distal part (Fig. 14.3). More precisely,

$$p_{ext}(x, t) = \begin{cases} 0 & x < \frac{L_c}{3} \\ k_c p_{LV}(t) \left(\frac{3x}{L_c} - 1 \right) & \frac{L_c}{3} \leq x \leq \frac{2L_c}{3} \\ k_c p_{LV}(t) & x > \frac{2L_c}{3} \end{cases} \quad (14.2)$$

where $p_{LV}(t)$ is the time-varying LV pressure (see Fig. 14.2), $L_c = 7$ cm is the length of the equivalent coronary vessel, x is assumed to be zero at the inlet, and k_c is a constant that determines the proportion of ventricular pressure to be applied as external pressure. For the left subendocardial equivalent vessel, $k_c = 1$, while $k_c = 0.2$ for the right subendocardial vessel, thus reflecting the fact that the right coronary arteries undergo less compression than the left. The cross-sectional area of the LCA and RCA at the inlet was taken as 0.21 and 0.18 cm², respectively, which is slightly larger than measurements performed *in vivo* at more distal sites, where the cross-sectional area would be somewhat smaller than at the coronary inlet [23,24]. The value of β for LCA and RCA was found by using the Young's modulus of the femoral artery [23] and a wall thickness of 0.08 cm.

14.2.2 Reflections

Before proceeding to understand how the aortic valve is embedded into the arterial network, it is useful to understand how reflections work within the network. It was shown in [Chapter 13](#) that whenever there is a change in characteristic impedance due to changes in vessel properties or branching, wave reflections occur. The characteristic impedance of a vessel relates the velocity or flow of a wave to the applied pressure (and is therefore analogous to Ohm's Law, i.e., $Z_0 = \frac{P}{Q}$) and may be expressed as

$$Z_0 = \frac{1}{Y_0} = \frac{\rho c_0}{A_0} \quad (14.3)$$

Considering [Eq. \(13.9\)](#), it can be seen that Z_0 depends only on vessel geometric and material properties. Y_0 is called the characteristic admittance. The reflection coefficient (R) is commonly used to express the ratio of the amplitudes of incoming and reflected waves and is given by [using the same subscripts as in [\(13.46\)](#)]

$$R = \frac{Y_{0p} - \sum_{i=1}^n Y_{0i}}{Y_{0p} + \sum_{i=1}^n Y_{0i}} \quad (14.4)$$

For a dead end terminal (i.e., $\sum Y_{0i} = 0$), there is a total positive reflection ($R = 1$) and for an opening with no downstream resistance ($\sum Y_{0i} \rightarrow \infty$), there is a total negative reflection ($R \rightarrow -1$), while for a well-matched branching no reflection occurs ($R = 0$). While [Eq. \(14.4\)](#) is strictly valid only in a linear model, it is useful for verifying the results of a nonlinear model and to make general predictions about reflections at discontinuities or vessel branching points. A reflection coefficient can also be used to set boundary conditions of simple resistance terminal vessels (see [Section 14.2.4](#)).

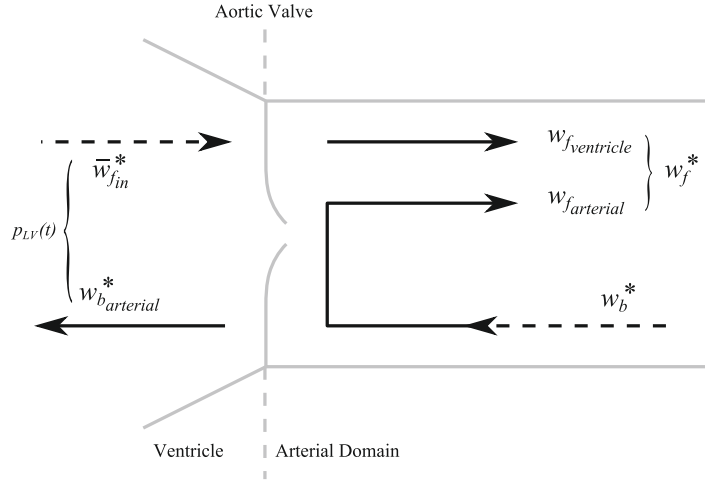
14.2.3 Aortic valve

The schematic describing the coupling between left ventricle (LV) and aortic valve (AV) is shown in [Fig. 14.4](#). The forward left ventricular pressure is generated using two sigmoid functions fused at the mid-ejection period as discussed previously. The left ventricle contraction gives rise to a forward characteristic variable and backward characteristic variable due to arterial effects while propagating through the arterial system as illustrated in [Fig. 14.4](#). The total forward characteristic variable, including the contribution from the aortic valve, can be written as

$$w_f^{*(n+1)} = w_{f_{ventricle}}^{(n+1)} + w_{f_{arterial}}^{(n+1)} \quad (14.5)$$

where $w_{f_{ventricle}}$ represents the forward characteristic variable of the ventricular pressure, which can be expressed as

$$w_{f_{ventricle}}^{(n+1)} = (1 - R_{av}) \bar{w}_{fin}^{*(n+1)} \quad (14.6)$$

**FIGURE 14.4**

A simple ventricular-valve model describing the transformation of the characteristic variables at the aortic valve.

where R_{av} denotes the aortic valve reflection coefficient and $(1 - R_{av})$ is known as the time-varying aortic valve transmission coefficient T_{av} . This transmission coefficient allows the forward characteristic variable to partially ($0 < T_{av} < 1$) or completely ($T_{av} = 1$) transmit through or completely reflect ($T_{av} = 0$) due to the presence of the aortic valve.

An exponential variation is appropriate for axial displacement waveforms of leaflet tips in normal aortic valves [25]. The valve function $V(t)$ used may therefore be expressed as

$$V(t) = B \left(e^{-kt} - 1 \right) \quad (14.7)$$

where $0 < t < 1$, while the constants are $B = 1/(e^{-k} - 1)$ and $k = 3$. This expression results in variation between 0 and 1 over 1 s. A scaled (in time or amplitude) and/or reversed version of this expression is then applied (in the form of reflection coefficient) to the opening or closing valve as necessary.

The term $w_{b,arterial}$ is associated with the backward characteristic variable which is completely transmitted ($R_{av} = 0$), or partially ($0 < R_{av} < 1$) or completely reflected ($R_{av} = 1$) from the aortic valve which yields

$$w_{f,arterial}^{(n+1)} = -R_{av} w_b^{*(n+1)} \quad (14.8)$$

Expanding $w_{f,b}^*$ gives the final form (Note that $w^* = w - w^0$)

$$w_f^{(n+1)} = w_f^0 + (1 - R_{av}) \left(\bar{w}_{fin}^{(n+1)} - w_f^0 \right) - R_{av} \left(w_b^{(n+1)} - w_b^0 \right) \quad (14.9)$$

where \bar{w}_f is calculated from the prescribed forward pressure using Eq. (13.28).

14.2.3.1 Afterload-corrected ventricular pressure

Afterload can be described as the pressure in the aorta that the heart needs to overcome in order to eject blood out of the heart. If the aortic pressure increases, the ventricular pressure increases and maintains the amount of blood that needs to be pumped through the arterial system. The afterload-corrected ventricular pressure can be described by rearranging Eq. (13.28) as

$$p_{LV}(t) = p_{ext} + \frac{\rho}{32} \left(\bar{w}_{fin}^{(n+1)} - w_{barterial}^{(n+1)} \right)^2 - \beta \sqrt{A_0} \quad (14.10)$$

where the backward characteristic variable w_b is caused by the backward-propagating waves transmitted into the left ventricle illustrated in Fig. 14.4 and can be obtained through

$$w_{barterial}^{*(n+1)} = (1 - R_{av}) w_b^{*(n+1)}$$

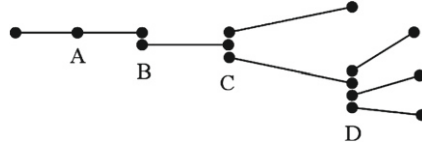
Expanding w_b^* gives (see Chapter 13)

$$w_{barterial}^{(n+1)} = w_b^0 + (1 - R_{av}) \left(w_b^{(n+1)} - w_b^0 \right) \quad (14.11)$$

14.2.4 Vessel branching

The arterial circulation has the structure of a tree, where blood from the LV is pumped into the aortic trunk, and major branches direct blood to all parts of the body, feeding fractal-like asymmetric networks [26] of small arteries, arterioles, and finally capillaries where oxygen and carbon dioxide transfer occurs. Deoxygenated blood then continues to the venous circulation, where small venules connect to progressively larger veins and finally return blood to the right side of the heart. The pulmonary circulation may be treated as a separate circulation, fed from the RV, which provides blood flow to the lungs. This circulation has a fractal structure [27,28] due to the rapid and almost immediate branching network that ends in the pulmonary capillaries. Here, blood is reoxygenated and completes its journey back to the left heart via the pulmonary venous circulation.

Modeling part or all of the circulation, therefore, requires consideration of branching points such as bifurcations or trifurcations. In one dimension, branching points are a type of discontinuity in cross-sectional area and vessel material properties (β). Figure 14.5 shows a variety of possible node connections. Type B has two nodes sharing the same location and the adjacent elements are therefore not connected in any intrinsic way. The benefit of such a connection is that unlike type A connections, true discontinuities can be realized, since for example, the co-located nodes can have different values of A_0 or β . In a similar way, bifurcations are formed by a connection of type C, with three co-located nodes belonging to the three weakly connected elements. A trifurcation would be of type D and indeed, any number of branches is possible.

**FIGURE 14.5**

Various possible nodal branching/connection types.

To transmit information between co-located nodes, the characteristic solutions will again be used. (Note: The following treatment is a generalization of that given in Refs. [29,30].) Consider a parent vessel p with N daughter vessels. Each of the $N + 1$ co-located nodes is treated as boundaries and the boundary conditions (i.e., values of A and u for each node) will be set using upstream and downstream information. There are therefore $2(N + 1)$ unknowns and as many equations required to solve the system. Half of these equations can be determined from the outgoing characteristics as discussed in Section 13.2.2. The known value of the characteristic can then be related to the primitive variables for the nodes as follows:

$$w_{1p} = u_p + 4A_p^{1/4} \sqrt{\frac{\beta_p}{2\rho}} \quad (14.12)$$

for the parent vessel and

$$w_{2i} = u_i - 4A_i^{1/4} \sqrt{\frac{\beta_i}{2\rho}} \quad (14.13)$$

for the i th daughter vessel. Note that it is possible to have multiple “parent” vessels, but for this example only a single parent vessel branching to multiple daughter vessels is considered. Next, equations are used that ensure continuity of mass flow and total pressure. These provide the necessary remaining information and so, in this case, the incoming characteristics are not needed. Conservation of mass provides one equation and requires that

$$Q = A_p u_p = \sum_{i=1}^N A_i u_i \quad (14.14)$$

Continuity of total pressure [i.e., dynamic pressure $(\rho u^2/2)$ + static pressure Eq. (13.6)] provides the remaining N equations, where for the i th daughter vessel,

$$\frac{\rho u_p^2}{2} + p_{ext(p)} + \beta (\sqrt{A_p} - \sqrt{A_{p0}}) = \frac{\rho u_i^2}{2} + p_{ext(i)} + \beta (\sqrt{A_i} - \sqrt{A_{i0}}) \quad (14.15)$$

This set of nonlinear equations may then be solved using the Newton-Raphson method [31].

14.2.5 Terminal vessels

The number of branches in the arterial tree increases dramatically toward the periphery, which includes approximately 2.7×10^9 capillaries [19]. While the vast number of small vessels and capillaries cannot be modeled individually, their combined effect may be approximated and imposed at the terminal boundaries of a model of larger arteries. Many investigators [2,3,6,29,32] have treated the downstream effects on flow as being purely resistive, that is, there is no phase difference between reflected pressure and flow, and the reflection coefficient is the same for all frequency harmonics. In this case, the change in the incoming characteristic could be determined from the change in the outgoing characteristic. For a wavefront traveling in the $+x$ direction the terminal reflection coefficient is

$$R_t = -\frac{\Delta w_2}{\Delta w_1} = -\frac{w_2^{n+1} - w_2^0}{w_1^{n+1} - w_1^0} \quad (14.16)$$

The value of w_1 for the next time step ($t = n + 1$) can be determined via extrapolation (see Section 13.2.3), while w_1^0 and w_2^0 are the initial values of the characteristic variables. The unknown (w_2^{n+1}) can then be determined by simply rearranging Eq. (14.16):

$$w_2^{n+1} = w_2^0 - R_t(w_1^{n+1} - w_1^0) \quad (14.17)$$

The drawback of the simple resistance terminal is that the arterial bed is known to have capacitive as well as resistive properties. This leads to a phase lag between reflected pressure and velocity and this means that higher frequency harmonics undergo smaller reflections. Thus the reflection coefficient is frequency dependant and complex [$R = R(j\omega)$]. This has led others [9–11,13] to use the Windkessel element (which consists of two resistors and a capacitor) as vessel terminals. Here, the input impedance and reflection coefficient spectra have peaks at zero frequency, fall rapidly over the first several harmonics, and remain small and relatively constant at high frequencies [33]. While this model is a vast improvement, Olufsen [33] points out that the Windkessel element does not take into account the effects of wave propagation in a branching network. The shortcoming is that in real branching networks there are ripples in the input impedance spectrum (and thus reflection coefficient) after the low frequency peak [2,26].

An alternative is to apply the input impedance of a generalized branching network model at the terminals [26,33]. While this produces ripples in the input impedance and input reflection coefficient spectra, the method relies on an assumption of linearity and is difficult to apply in a nonlinear time-domain model.

14.2.5.1 Tapering vessels as terminal elements

Another possible approach is to use a tapering vessel as the terminal element. Consider a vessel with multiple step decreases in A_0 or step increases in β . Each step corresponds to a local increase in characteristic impedance (Z_0) and thus reflections will occur at each stepping point. Since these reflections occur at different distances

along the vessel, backward-running waves will reach the start of the vessel at different times. Note however that waves traveling back toward the inlet will also experience partial and negative re-reflections, since in this direction there are step decreases in characteristic impedance. Thus, from the perspective of the inlet, reflections that occur at more distant reflection sites have a smaller effect. This is similar to what occurs in the arterial system. Forward-traveling waves undergo relatively small reflections at branching points, but backward-traveling waves undergo relatively large negative re-reflections. In the limit where there is an infinite number of very small steps, there will be an infinite number of small reflections and re-reflections at every point along the vessel. It is thus possible to approximate the behavior of a branching network at its input with a single tapering vessel. In fact, several investigators [34–37] have modeled the input characteristics of the entire arterial tree with some success using only one or two tapering vessels. These models predict an input impedance spectrum with ripples which is similar to the input characteristics of branching networks. An exact solution to the Riccati equation which governs the input impedance of a tapering vessel has only recently been formulated [38]. This and other approximate solutions [35–37] assume linearity and ignore viscous effects, which become important in small vessels. No known analytical solution exists for the input impedance of a tapering vessel for nonlinear viscous flow. An empirical approach has thus been taken in the study described in this chapter and the relationship between input reflection coefficient, vessel length, and taper gradient (a linear taper is assumed throughout) has been investigated. The frequency-dependent input reflection coefficient, $R_{in}(j\omega)$, of both a fourth-generation branching network and various tapering vessels was determined by prescribing sinusoidal forward pressures of various frequencies at the inlet (1–10 Hz in steps of 1 and 12, 15, 20, 25 Hz). Since this input was a time-varying *forward* pressure, the time-varying backward pressure (which arises from reflections) was determined by subtracting the actual (or assigned) value of pressure (see [Section 13.2.3](#)) at the inlet from the forward pressure. Thus for each sinusoidal inlet forward pressure, the inlet backward pressure was calculated, which, after an initial stabilization period, was also sinusoidal with the same frequency as the forward pressure. The magnitude of the effective input reflection coefficient was then calculated for each frequency as the ratio of the amplitudes of the forward and backward sine waves. The phase was also determined via the time delay between the occurrence of peaks in the forward and backward sine waves. The results are then compared to get the most suitable tapering vessel.

Note that a boundary condition still needs to be specified at the end of the tapering vessel. This boundary condition can be set by using a pure resistance or a Windkessel impedance (as discussed above). For simplicity, the terminal (or load) impedance of each tapering vessel has been chosen to provide good matching. To achieve this, a reflection coefficient of zero is applied according to [Eq. \(14.16\)](#). While using a Windkessel load impedance at the output would result in more degrees of freedom for adjusting the input characteristics of the tapering vessel, setting a zero reflection coefficient at the output means that the input characteristics of the tapering vessel can be determined entirely by the length of the vessel and the gradient (or severity) of the taper [14].

14.2.6 Numerical solution

The fluid dynamics equations and solution procedure are identical to that explained in [Chapter 13](#). The difference here is that the one-dimensional fluid–structure interaction method is applied to a network of one-dimensional tubes along with appropriate properties, initial conditions, boundary conditions, and other conditions, mentioned previously. The step-by-step procedure of model integration is given below.

14.2.6.1 Initialization

1. Using the ventricular input waveform calculate the incoming characteristic wave at the inlet for each time step [[Eq. \(13.28\)](#)].
2. Calculate the valve opening and closing function [[Eq. \(14.7\)](#)].
3. Calculate an external pressure weighting factor for each node in the subendocardial coronary “equivalent” vessels [[Eq. \(14.2\)](#)].

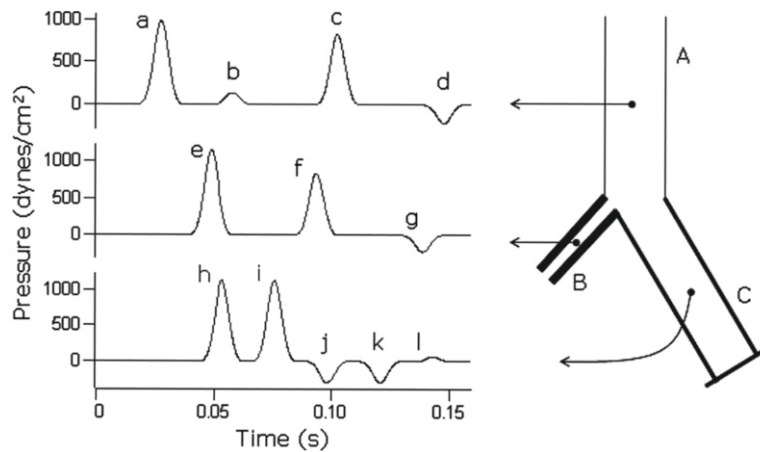
14.2.6.2 The main processing within the time-stepping loop follows

1. Using the value of afterload-corrected ventricular pressure (p_{LV}) from the previous time step (or initial value for the first iteration), calculate the external pressure for each node of the subendocardial coronary vessels [[Eq. \(14.2\)](#)].
2. Solve the governing equations using the method presented in the previous chapter.
3. Calculate the outgoing characteristic wave at the inlet [[Eq. \(13.28\)](#)].
4. Based on the values of pressure and flow in the previous time step, calculate the valve reflection and transmission coefficients (R_{Vr} and T_{Vp}) (see [Section 14.2.3](#)).
5. Using the prescribed incoming (ventricular) characteristic wave (Step 1) and the valve coefficients (Step 7), calculate the incoming (aortic) characteristic wave [[Eq. \(14.5\)](#)].
6. Based on the incoming and outgoing characteristics, calculate and assign the boundary conditions at the inlet (see [Section 13.2.3](#)).
7. Calculate the afterload-corrected ventricular pressure [[Eq. \(14.10\)](#)].
8. For each discontinuity or branching point (i.e., bifurcation, trifurcation, etc.), calculate the conditions for all co-located nodes (see [Section 14.2.4](#)).
9. For all tapering terminal vessels, calculate the outgoing characteristic [[Eq. \(13.27\)](#)]. Using a reflection coefficient of zero, calculate the incoming characteristic and the boundary conditions for each outlet.

The examples below are generated using the steps discussed above.

Example 14.1. Vessel branching

The branching nature of the arterial tree and the fact that parent and daughter branches are not perfectly matched [[Eq. \(14.4\)](#)] gives rise to a great number of reflections, re-reflections, and so on throughout the system. To illustrate this, [Fig. 14.6](#) shows the propagation of a short pressure pulse in a single bifurcation. The parent vessel (A) ($A_0 = 4$, $\beta_A = 113487$, $L = 10$) branches into a narrow open-ended branch (B) ($A_0 = 0.5$, $\beta_B = 4\beta_A$, $L = 5$) and a larger close-ended branch (C) ($A_0 = 0.35$, $\beta_B = 2\beta_A$, $L = 10$). When pressure is monitored midway along each

**FIGURE 14.6**

Pulse propagation in a single bifurcation. The pulse propagates from parent branch A to daughter branches B (with a terminal reflection coefficient $R_t = 0$) and C ($R_t = 1$). Pressure is monitored at the midpoint of each vessel and plotted against time, showing the primary and reflected waves that occur (see text for explanation). The line thickness of the vessels signifies wall stiffness (i.e., $\beta_B = 4\beta_A = 2\beta_C$).

branch, it can be seen that a single input pulse (*a*) gives rise to several reflected waves in each segment in addition to the primary wave. The first reflection occurs when the wave reaches the bifurcation, partly reflecting back along A (wave *b*) and partly transmitting to both daughter branches (*e* and *h*). In branch B, wave *e* arrives at the monitoring point before wave *h* in branch C, due to the shorter distance and greater wave speed in B. Since B is well matched to any downstream vessels (that is, the terminal reflection coefficient is zero), there are no further reflections of wave *e*. Conversely, wave *h* in C reflects completely at the closed end, producing *i*, which has the same magnitude. This backward-running wave then propagates toward the bifurcation, reflecting once again to produce the forward-running wave *j* in C, the backward-running wave *c* in A, and the forward-running wave *f* in B. Note that the effective reflection coefficient of the bifurcation from the perspective of C is negative (since the combined characteristic impedance of A and C is less than that of B), causing wave *j* to be negative. This re-reflected wave is reflected again at the terminal of C producing *k*, which is then partially reflected once again as *l* and transmitted as waves *g* and *d*.

Several points should be noted. First, the input pulse is very short to enable clear view of backward- and forward-running waves without overlap. The heart pulse however is much longer making individual waves more difficult to distinguish. It is then important to note that the principle of superposition, where the overlapping waves can simply be considered as the sum of individual waves, is only valid in a linear model. In nonlinear models, this is not the case and will only hold approximately. This is because linear models assume a constant wave speed whereas nonlinear

models do not. Thus a wave traveling by itself will propagate at a different speed to the same wave when it encounters other waves [39]. Therefore, forward-running waves do in fact influence backward-running waves, although this effect is small. Secondly, the results in Fig. 14.6 are for inviscid flow. For viscous flow there would be some attenuation of the waves which, in turn, would lead to a slightly lower peak wave speed. However since the signals in Fig. 14.6 are small, these effects are negligible.

Example 14.2. Normal “at rest” state

Figure 14.7 shows various waveforms for a normal adult at rest. The model produces waveforms that contain all the well-known features that are obtained from

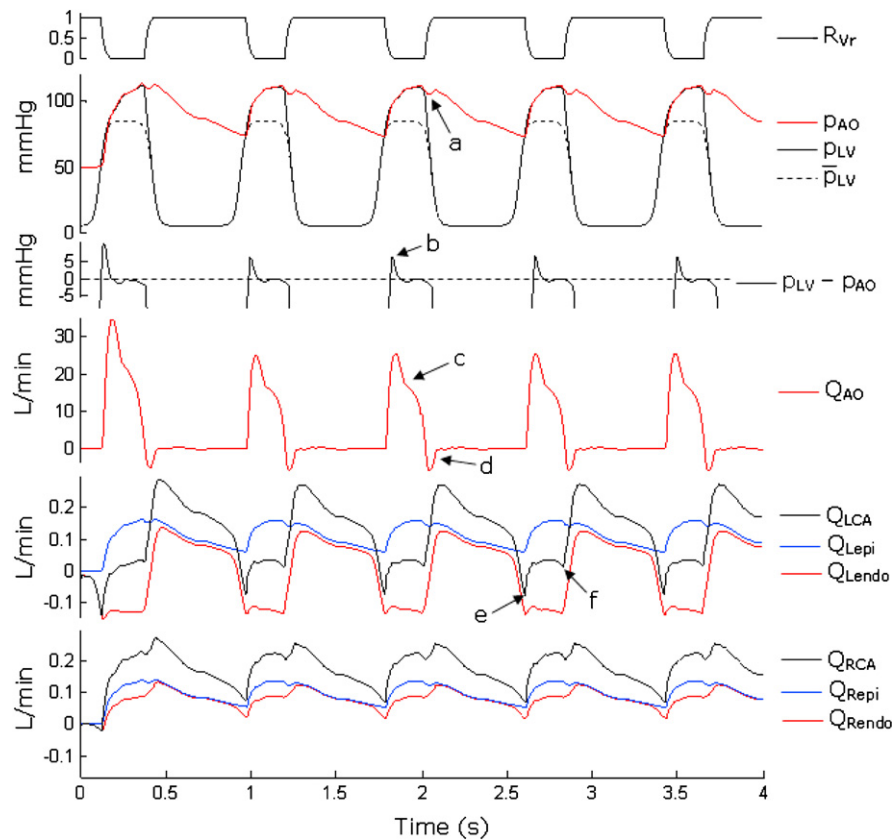


FIGURE 14.7

Waveforms produced by the model representing a normal human adult at rest. Marked features are (a) the aortic valve closure notch, (b) early systolic ventricule-aorta pressure gradient, (c) the reduction in blood flow due to reflected waves in mid-systole, (d) aortic backflow during valve closure, and (e) the first and (f) second local minima of left coronary flow (see text for explanations).

in vivo measurements, with regularity arising after the first beat. The plot of aortic valve reflection coefficient (R_{Vr}) shows that the valve opens and closes at the appropriate times based on local hemodynamics as discussed in Section 14.2.3. Prescribed (\bar{p}_{LV}) and afterload adjusted (p_{LV}) LV pressure are shown along with ascending aortic pressure (p_{AO}) and aortic flow (Q_{AO}), all of which display normal morphologies [40,41]. It can be seen that during systole, afterload has the effect of increasing ventricular pressure. Also during systole, p_{AO} is almost equal to p_{LV} , with a small positive pressure difference ($p_{LV} - p_{AO}$) in early systole (marked feature b) which drives forward flow, and a small negative pressure difference in mid-to-late systole caused by backward-running waves and the relaxing ventricle, which cause reductions in aortic flow and lead to valve closure. Relatively early in systole, there is a pressure-increasing and flow-decreasing hump in p_{AO} and Q_{AO} (feature c). This is the well-known pressure augmentation [42] that is due to reflected waves arriving at the aorta and causes the shape of p_{LV} and p_{AO} waveforms to depart from that of \bar{p}_{LV} . Valve closure is associated with the dicrotic notch in p_{AO} (feature a). This jump in pressure can be explained by noting that the valve reflection coefficient is rapidly increasing during this time and thus backward-running waves begin to reflect from the valve. At this time there is also a small amount of reverse flow across the valve. During diastole, Q_{AO} is effectively zero while p_{AO} gradually declines. This decline is governed by reflected waves. Using the data shown in Fig. 14.7, the common hemodynamic measures of systolic/diastolic(mean) aortic pressures of 110/73(94), cardiac output ($CO = \text{mean } Q_{AO\text{root}}$) of 4.5 L/min, contractility index (maximum dp_{LV}/dt) of 1179 mmHg/s, and systemic vascular resistance ($SVR = \text{mean } p_{AO}/CO$ with central venous pressure taken to be zero) of 1671 dynes/s/cm⁵ would all be considered normal for an adult human at rest.

The morphology of coronary flow also accords with *in vivo* data. Mean flow in the LCA and RCA was 0.127 and 0.181 L/min, respectively, with total coronary flow accounting for 6.8% of cardiac output, which again is in the range of normal values. In the LCA, the majority of flow (Q_{LCA}) occurs during diastole [19,43,44] and there are two well-defined local minima [19,22]. To explain these features, it is helpful to observe that Q_{LCA} is equal to the sum of subepicardial and subendocardial flows (Q_{Lepi} and Q_{Lendo}). Q_{Lepi} has a similar morphology to aortic pressure which shows that forward-running waves are predominant throughout the cardiac cycle. In contrast, Q_{Lendo} reveals a large amount of backflow during systole when the heart squeezes blood out of the subendocardial equivalent vessel, while during diastole when there is almost no external pressure applied, Q_{Lendo} follows Q_{Lepi} . Such large subendocardial backflows have been observed in [45]. The first minimum (feature e) in Q_{LCA} occurs in early systole and is caused by the fall in Q_{Lendo} . The presence of reverse flow in Q_{LCA} thus depends on whether the negative Q_{Lendo} outweighs the positive end-diastolic Q_{Lepi} . The Q_{LCA} second minimum occurs at the time of valve closure and is accompanied by decreases in both Q_{Lepi} and Q_{Lendo} . This is most likely associated with the fact that Q_{AO} falls rapidly just before the external pressure is removed and Q_{Lendo} begins to rise. In the right coronary circulation, Q_{RCA} , Q_{Repi} , and Q_{Rendo} always remain positive [46], since the external pressure

exerted on subendocardial vessels is less pronounced. The effect of external pressure is seen, however, by the reduced flow in Q_{Rendo} compared with Q_{Repi} during systole.

Example 14.3. Exercise and disease conditions

Exercise is characterized by an increase in heart rate, force of ventricular contraction, and peak pressure. Systemic vascular resistance also drops because more small blood vessels are recruited for oxygen transfer [47]. To simulate moderate exercise, the model parameters were adjusted as follows: $HR = 115$ bpm, $\bar{p}_{LV} = 115/5$ mmHg, and $RVOT = RVCT = 35$ ms. Vascular resistance was reduced by decreasing the taper severity of terminal elements so that $A_0(L) = 0.1$ cm² or $0.9A_0(0)$, whichever was smaller. Figure 14.8b shows a regular beat under these conditions and may be compared to the “at rest” case in Fig. 14.8a. Of particular note is a 3.3-fold increase in cardiac output and an associated increase in coronary flow. There is also an increase in peak $p_{AO} - p_{LV}$ to 17.8 mmHg (compared with 6.7 mmHg at rest). Contractility also increased by 133%. These results accord well with *in vivo* measurements [47].

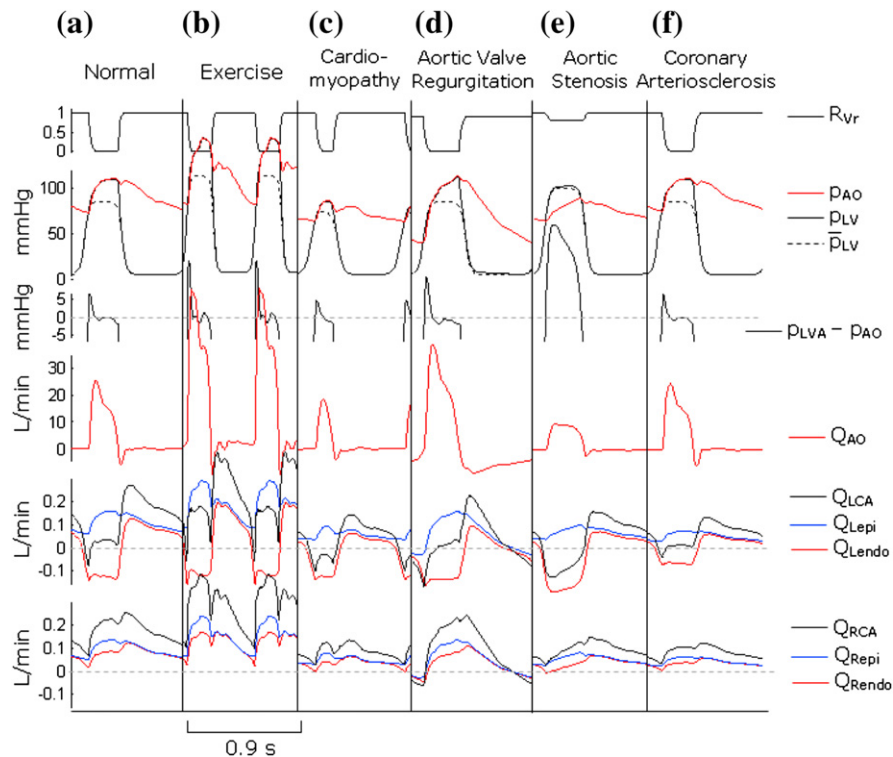


FIGURE 14.8

Sample steady-state beats from simulations of various normal and disease states.

Cardiomyopathy may take several forms but is generally characterized by a reduction in the capacity of the heart to generate force. Accordingly, peak \bar{p}_{LV} was reduced to 60 mmHg, while the isovolumic contraction and relaxation times were increased by 30% compared with the normal “at rest” case. Figure 14.8c shows that cardiomyopathy has the opposite effect to exercise in a normal heart, with cardiac output dropping to 1.79 L/min, contractility dropping by 47% and $p_{AO} - p_{LV}$ dropping by 43%. Similar trends have been observed in [48]. While [48] showed only small reductions in left coronary flow, the model predicted a 64% decrease. This may reflect that the amount of external pressure applied by the failing heart is actually less than applied in the model.

Compromise of the structural integrity of the aortic valve can lead to leakage of blood from aorta to ventricle during diastole. To model mild valve regurgitation, the maximum valve reflection coefficient was set to $R_{Vr}(\max) = 0.9$. This led (Fig. 14.8d) to sustained Q_{AO} backflow during the whole period of diastole, and although peak Q_{AO} was higher, cardiac output fell by 37%. Valve leakage also led to a small amount of negative flow in Q_{Lepi} as well as both right coronary flows. End-diastolic and mean p_{AO} fell while peak p_{AO} was preserved [40/114(76)] and peak $p_{AO} - p_{LV}$ increased by 64%. These findings are in good agreement with [49].

Aortic valve stenosis (or just “aortic stenosis”) is a narrowing of the aortic valve which impedes systolic flow. This leads to a significant pressure gradient between the LV and the aorta, and to compensate, the LV must generate much greater pressures to maintain adequate arterial pressures and flows. This may be modeled with a reduced maximum valve transmission coefficient or nonzero reflection coefficient during systole as well as an increased \bar{p}_{LV} . Using $R_{Vr}(\min) = 0.8$ and $\bar{p}_{LV} = 100/5$, Fig. 14.8e reveals a large ventricular-aortic pressure gradient (peak $p_{AO} - p_{LV}$ of 26 mmHg compared with 6.7 mmHg in the normal state) which lasts for all of systole. Despite the increased ventricular pressure, aortic pressure is lower [64/89(77)], and this leads to compromised coronary flow. Due to increased external pressure during systole, there is a greater negative Q_{Lendo} which overcomes Q_{Lepi} and is revealed in Q_{LCA} as a sustained systolic backflow. These trends have been observed by Kenny et al. [50] and Sabbah et al. [51].

Coronary arteriosclerosis is a stiffening of the coronary vessel walls due to the deposition of lipids, lipid by-products, and calcium. To provide a basic model of arteriosclerosis, Young’s modulus of the coronary vessels was increased by a factor of 4. Since this is equivalent to a reduction in characteristic admittance (see Section 14.2.2), mean Q_{LCA} and Q_{RCA} fell by 52% and 46%, respectively (Fig. 14.8f) [19], although there was little change to the morphology of coronary flow. Systemic hemodynamics did not change significantly, although in reality, the reduced coronary flow would lead to compromised ventricular function and thus hemodynamics in general. To model this interaction, cardiac metabolism and gas transport between myocardium and coronary capillaries would need to be accounted for.

In summary, various normal and disease states have been simulated. While the model does not account for all physiological interactions or physical characteristics

of the diseases, the waveforms obtained from the model are consistent with *in vivo* measurements and suggest that the model is physiologically relevant.

14.3 Image-based subject-specific flow modeling

The general structure of any subject-specific blood flow modeling framework consists of mainly image segmentation, meshing, and solution stages. The image segmentation is normally followed by a meshing stage in which a domain discretization is carried out. The connection between the image processing and meshing is established via a geometry definition step. The majority of the efforts during the mesh generation process goes toward establishing a valid and high-quality surface mesh that is a close representation of the geometry. The surface meshing in general is followed by the boundary layer mesh construction and artery wall meshing (when applicable). The boundary layer and arterial wall volume discretizations are followed by automatic volume meshing of the central flow domain of the artery with unstructured meshes. The flow solver is then used along with appropriately generated boundary conditions to complete the pipeline. The solver may include rigid geometry, flow and structure coupling, and Newtonian or non-Newtonian approximation and may also include multiscale mechanics or turbulence.

One of the main challenges in the computational modeling of hemodynamics is the accurate reconstruction of a blood vessel geometry. Anatomically accurate geometric models of the lumen are essential for realistic flow simulations and analysis. The anatomical information used to reconstruct the geometries are usually provided in the form of medical image datasets (scans) from imaging modalities such as computed tomography (CT) and magnetic resonance (MR) imaging. Manual reconstruction of the geometries can be tedious and time consuming. There is also the issue of variability between the geometries extracted manually by different individuals, and variability of geometries extracted by the same individual on different occasions. In order to allow computational flow modeling to be efficiently applied as a diagnostic or predictive tool, the amount of user intervention required in the process should be reasonably small. Therefore, a robust and efficient method that can be used to accurately segment the geometry from medical image datasets can be very useful and advantageous in the modeling process.

Assuming that a reasonably accurate reconstruction of the geometry is possible, the next stage of the modeling pipeline would be to generate a surface mesh or meshes to accurately discretize the surface or surfaces of the geometry. Unlike well-defined standard engineering geometries, the reconstructed subject-specific, arterial geometries are often defined by binaries. Thus, an alternative approach is required to that of standard engineering applications. Once a valid mesh is generated, appropriate flow conditions from either measurements or assumed data should be generated before flow algorithm is applied to get a solution.

14.3.1 Image segmentation

Extracting geometry from 3D scan data is a prerequisite for many computational modeling applications in cardiovascular fluid dynamics. Ideally, it should be carried out with minimum user interference and should robustly handle variations and noise interference that exist in the imaging data. Although a large number of procedures are available for image segmentation, a level set based image segmentation technique [52,53] to extract arterial geometries is adopted. An overview of this method and implementation details are given below. Let $I(\mathbf{x})$ denote the 3D gray image, where $\mathbf{x} = [x, y, z]^T$ is a point in the image domain \mathcal{D} . Let Ω be an object to be segmented from this image. We employ the level set method in which the object boundary $\partial\Omega(t)$ is defined through the level set function $\Phi(\mathbf{x}, t)$:

$$\partial\Omega(t) = \{\mathbf{x} : \Phi(\mathbf{x}, t) = 0\} \quad (14.18)$$

To compute the level set function, we numerically solve the following PDE for $\Phi(\mathbf{x}, t)$ [52,53]:

$$\frac{\partial\Phi}{\partial t} = \alpha g(\mathbf{x})\kappa(\mathbf{x}, t)|\nabla\Phi| - (1 - \alpha)(\mathbf{F}(\mathbf{x}) \cdot \nabla\Phi) \quad (14.19)$$

where α is a tuning parameter, $g(\mathbf{x}) = 1/(1 + |\nabla I|)$ is an edge stopping function, $\kappa(\mathbf{x}, t) = \nabla \cdot (\nabla\Phi/|\nabla\Phi|)$ is the mean curvature of the surface $\Phi = \text{const}$, and $\mathbf{F}(\mathbf{x}) = [F_x, F_y, F_z]^T$ is the flow function determined by image I . The flow function, which is derived from the image data, acts as an external force on the deformable model, and it is the most critical component in this kind of deformable model formulation.

14.3.2 Geometrical potential force (GPF)

The geometrical potential force (GPF) [52,53] is defined as

$$\mathbf{F}(\mathbf{x}) = \pm \frac{\nabla\Phi(\mathbf{x})}{|\nabla\Phi(\mathbf{x})|} G(\mathbf{x}) \quad (14.20)$$

where the scalar potential G is represented by a convolution of the form

$$G(\mathbf{x}) = P.V. \cdot \frac{\mathbf{x}}{|\mathbf{x}|^{\lambda+1}} * \nabla I(\mathbf{x}) = P.V. \cdot \iint_{\mathbf{x}' \in \mathcal{D}} \frac{\mathbf{x} - \mathbf{x}'}{|\mathbf{x} - \mathbf{x}'|^{\lambda+1}} \cdot \nabla I(\mathbf{x}') d\mathbf{x}' \quad (14.21)$$

Here $P.V.$ denotes the principle value and parameter λ depends on the domain dimension: $\lambda = 3$ for a 3D domain and \mathbf{x}' indicates a deformable model. Force, \mathbf{F} , acts in the direction of the gradient of Φ , i.e., always normal to the active surface $\Phi(\mathbf{x}, t) = 0$. It is possible to show that in the 2D case, with $\lambda = 2$, this force coincides with a magnetic-active force [54], but in contrast to magnetic force the GPF can be defined and applied to images of any dimension (even to 4D, i.e., time-varying 3D scans).

A discrete analog of the convolution kernel in the Eq. (14.21) takes the form

$$P.V. \frac{\mathbf{x}}{|\mathbf{x}|^{\lambda+1}} = \begin{cases} \mathbf{x}/|\mathbf{x}|^{\lambda+1} & \mathbf{x} \neq \mathbf{0} \\ \mathbf{0} & \mathbf{x} = \mathbf{0} \end{cases} \quad (14.22)$$

The fastest way to evaluate convolution (Eq. 14.21) and compute the potential $G_{ijk} = G(x_i, y_j, z_k)$ is to apply the 3D fast Fourier transform (FFT) method. It can be computed prior to the level set function calculation.

14.3.3 Numerical solution, initial and boundary conditions

Equation 14.19 may be solved using any standard method discussed in Chapter 2. The obvious and direct choice of numerical method is the finite difference method due to the fact that a regular mesh exists in the form of scan voxels. However, the finite element method can also be used on these regular meshes.

To set the initial condition, we have to define the initial surface S_0 somewhere in the vicinity of the blood vessel being investigated. An initial level set function is defined as a signed distance $D[S_0]$ from the initial surface S_0 , i.e.,

$$\Phi(x_i, y_j, z_k, 0) = D[S_0]$$

The signed distance can be computed efficiently using the algorithm described in Ref.[55]. At the boundaries of the image domain, zero Neumann boundary conditions are imposed. The narrow band approach described in [56] is used to reduce the computational cost in updating the level set function.

During the calculation, the function Φ may become irregular. Therefore, it is periodically reinitialized to the signed distance surface set from the current zero level set (surface of the deformable body), $S(t) = \{\mathbf{x} : \Phi(\mathbf{x}, t) = 0\}$. Hence, Φ can be redefined as $\Phi(\mathbf{x}, t) = D[S(t)]$, which is a smooth function with $S(t)$ being the surface with zero level set.

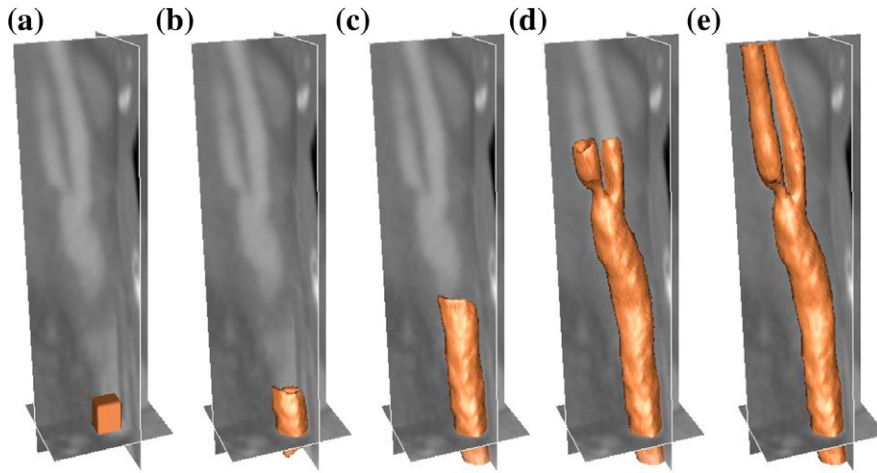
Example 14.4. Segmentation of a carotid artery

Here, a CT scan (DICOM dataset) of a human carotid artery is used to demonstrate the GPF-based segmentation method. The progression of the level set function is depicted in Fig. 14.9. Note that the initial model is positioned across the object boundaries to illustrate the capability of the deformable model to handle arbitrary cross-boundary initializations. The final solution is independent of the initial surface shape (example: sphere, parallelepiped, etc.). The position of the center of the initial surface S_0 is prescribed manually, which is the only manual operation in the segmentation process.

14.3.4 Domain discretization

14.3.4.1 Surface meshing

The surface mesh generation procedure has the following steps. The level set functions calculated by the image segmentation method are used to determine the skeleton of the

**FIGURE 14.9**

Segmentation of a carotid artery using GPF-based deformable model: (a) initial surface S_0 , after (b) 11, (c) 81, (d) 187, and (e) 241 time steps.

given artery first. This involves determining the approximate axis of the artery and its branches. This is followed by the procedure of generating a valid surface triangulation using again the final level set functions generated by the image segmentation. After carefully applying cosmetics to the surface mesh, it is clipped at the required length, orthogonal to the vessel axis.

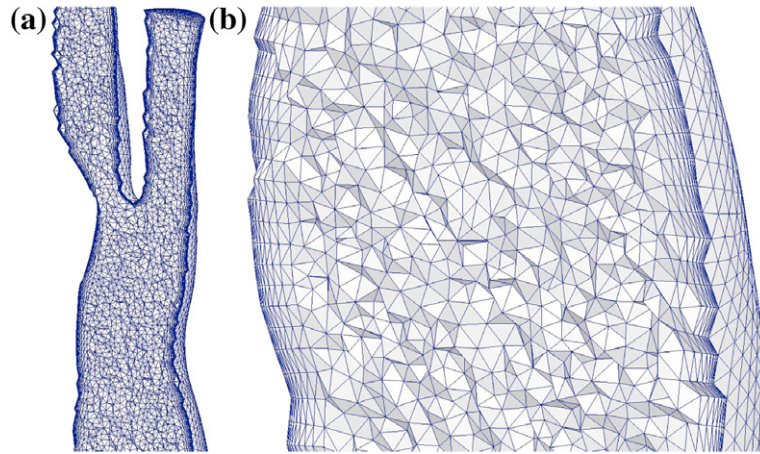
14.3.4.2 Boundary layer meshing

Often a boundary layer mesh is required close to the walls to capture high velocity gradients. This is generally carried out by growing inward normals from the surface triangles to create prism elements within the boundary layers. These prisms are then divided into tetrahedron elements if required.

14.3.5 Flow solution

In this section, analysis of flow in a moderately stenosed (blocked) carotid artery is presented. Any standard incompressible flow solver is sufficient to obtain a flow solution. Here, we recommend the CBS method and its variants. The geometry used here is generated using the image segmentation method presented in [Section 14.3.1](#), and the surface and volume meshes are obtained by employing all the techniques discussed in [Section 14.3.4](#). The transient flow boundary conditions are generated using the methods outlined in [Ref.\[57\]](#).

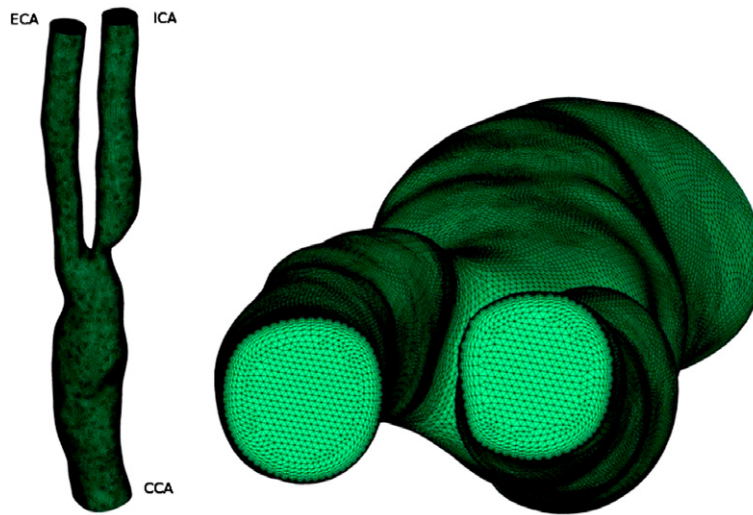
The carotid artery geometry used here was obtained from the Heart and Lung Centre, at Wolverhampton Hospital. This artery contains a moderate stenosis within the internal carotid artery (ICA) immediately downstream of the bifurcation. For the

**FIGURE 14.10**

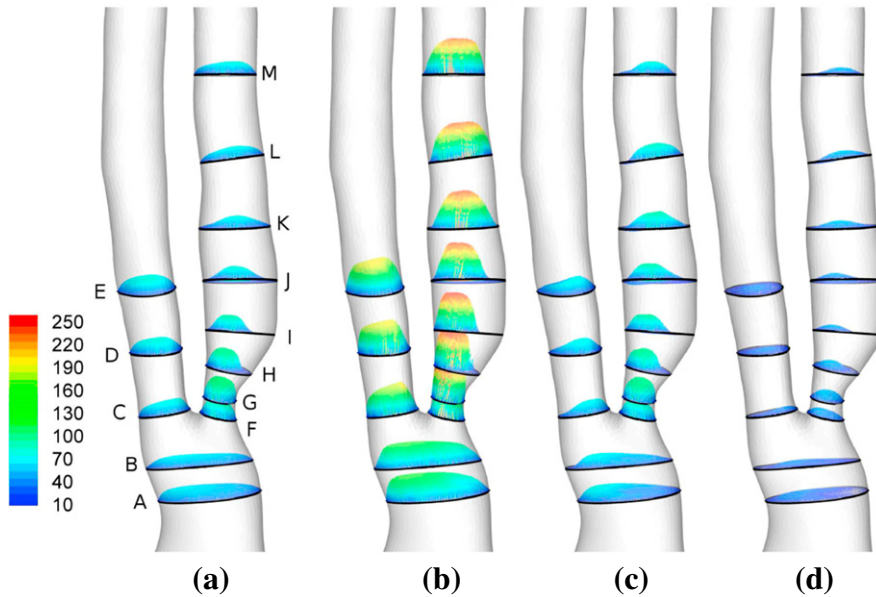
Volume mesh generated for a carotid artery.

numerical simulation, the mesh is clipped at the mid-height of the common carotid artery and maximal lengths of both internal and external carotid arteries are retained (see Fig. 14.10a). The final mesh is depicted in Fig. 14.11. This mesh consists of 4,126,777 linear tetrahedral elements and 708,191 nodes with 10 structured boundary layers. The stenosis occludes approximately 65% of the ICA. The common carotid artery (CCA) and the external carotid artery (ECA), however, are typical healthy arteries. A flow division of 50–50% between ECA and ICA is assumed. In normal circumstances, a flow division of 40–60% between ECA and ICA may be used. Since the ICA is partially occluded in the geometry used here, we assumed a 50–50% flow division.

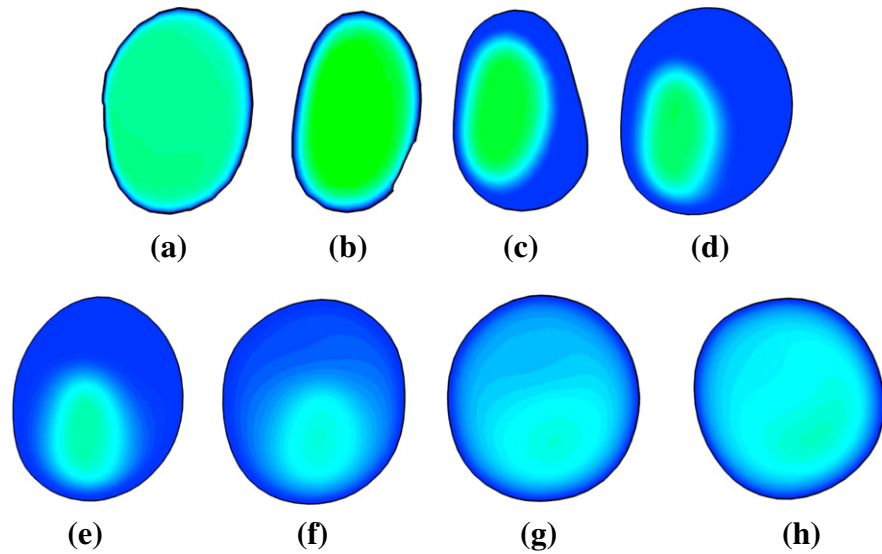
To examine the complex flow patterns within the stenosed artery and bifurcation in greater detail, the flow is visualized through a number of slices in Fig. 14.12. Here, the velocity vectors for the representative phases of the cardiac cycle (mid-acceleration, peak flow, mid-deceleration, diastolic notch) are shown. From the figure, it is clear that the stenosis has a strong influence on the downstream flow. This is shown by the flow separation and recirculation between the bifurcation and at least up to slice J. As a result, low wall shear stress (WSS) would be expected downstream of the stenosis, marking a potential region of further plaque formation. This is in good agreement with Smedby [58] who found that plaque was more likely to grow downstream of a stenosis. Within the CCA and ICA, the flow at mid-acceleration and peak flow is typically well distributed within the slice, although in the ECA the flow is skewed toward the inner wall. It is during deceleration that the skewed nature becomes more obvious, with larger velocity values found closer to the inner wall in the ECA. To further establish the flow conditions within the ICA, the slices are now presented for three time instances. The mid-acceleration time instance is presented in Fig. 14.13, peak flow in Fig. 14.14, and during deceleration in Fig. 14.15. From the three figures, it is possible to see the evolution of the flow during systole. During the mid-acceleration

**FIGURE 14.11**

Mesh used for the computation.

**FIGURE 14.12**

3D velocity distribution within 13 slices (cm/s): (a) mid-acceleration; (b) peak; (c) mid-deceleration; (d) aortic notch.

**FIGURE 14.13**

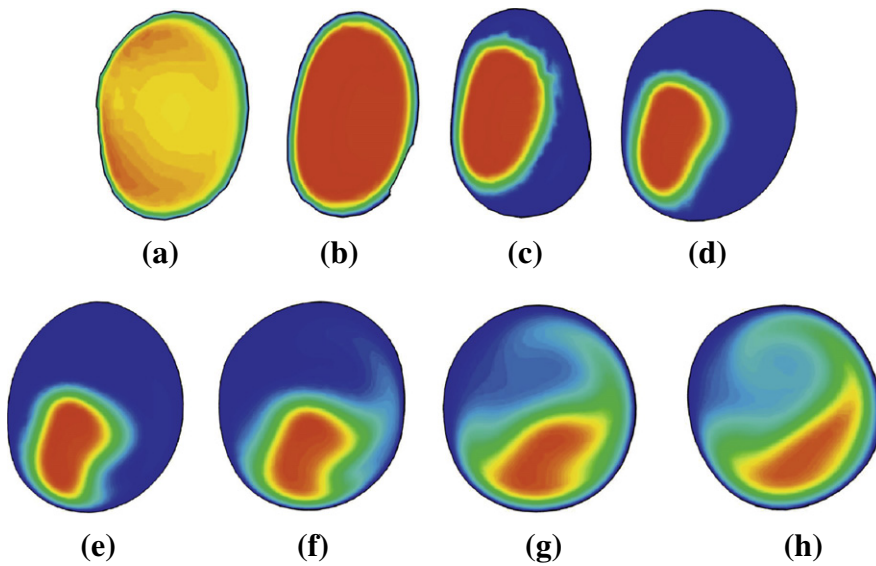
Streamline velocity magnitude at eight cross-sections within the ICA at mid-acceleration (cm/s): (a) slice F; (b) slice G; (c) slice H; (d) slice I; (e) slice J; (f) slice K; (g) slice L; (h) slice M.

stage, flow maintains a strong jet from slice F to slice J, before it begins to diffuse, and by slice M reattachment has occurred. In contrast, during peak flow the length of the jet has extended such that it impacts the posterior wall and flow is skewed toward this wall even in slice M. During peak flow, the predicted overall peak velocity is 266 cm/s within slice G and even in slice M, the velocity readily exceeds 200 cm/s. Within the deceleration phase, the influence of the jet is still strong, although secondary flow is observed downstream of the stenosis.

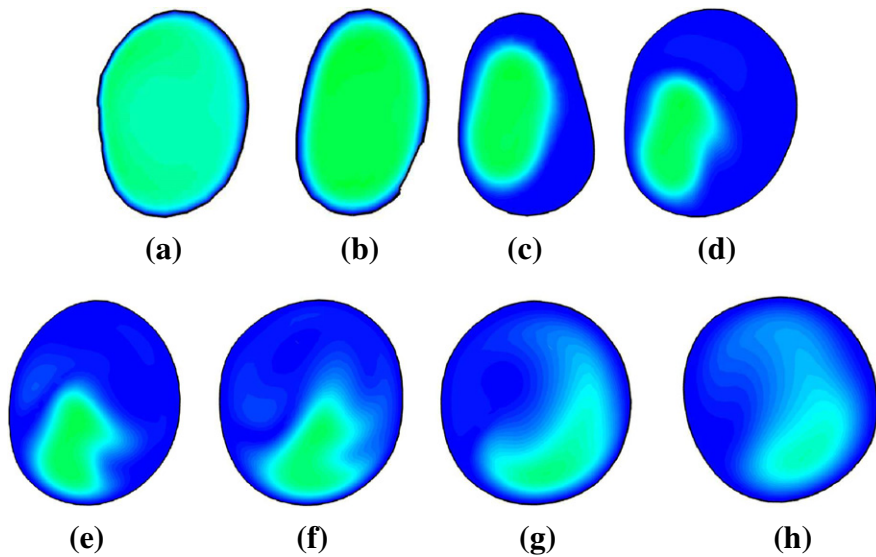
Low WSS is one of the indicators of the location of atherogenesis [59–66]. The work [67] defines the low shear stress as any value less than 5 dyne/cm² and this work also defines an athero-protective region as the region where the wall shear stress exceeds 25 dyne/cm². While instantaneous WSS values can provide individual snapshots of potential atherogenesis and athero-protective regions, the time-averaged WSS is employed to provide information over the full cardiac cycle. The time-averaged WSS can be determined using

$$\tau_{abs} = \frac{1}{T} \int_0^T |\mathbf{t}_s| dt \quad (14.23)$$

where $\mathbf{t}_s = \mathbf{t} - (\mathbf{t} \cdot \mathbf{n})\mathbf{n}$ is the surface traction vector and the traction vector \mathbf{t} is calculated from the Cauchy stress tensor $\boldsymbol{\sigma}$ and the surface normal vector \mathbf{n} using $\mathbf{t} = \boldsymbol{\sigma} \cdot \mathbf{n}$. The oscillatory shear index (OSI), originally introduced in [59] and adapted for general three-dimensional use in [68], is also used here to quantify the transient

**FIGURE 14.14**

Streamline velocity magnitude at eight cross-sections within the ICA at peak flow (cm/s): (a) slice F; (b) slice G; (c) slice H; (d) slice I; (e) slice J; (f) slice K; (g) slice L; (h) slice M.

**FIGURE 14.15**

Streamline velocity magnitude at eight cross-sections within the ICA at mid-deceleration (cm/s): (a) slice F; (b) slice G; (c) slice H; (d) slice I; (e) slice J; (f) slice K; (g) slice L; (h) slice M.

shear stress dynamics experienced by the endothelial cells. The OSI is a ratio of the absolute wall shear stress and the mean wall shear stress. The mean wall shear stress is calculated as the magnitude of the time-averaged surface traction vector $\tau_{mean} = \left| \frac{1}{T} \int_0^T \mathbf{t}_s dt \right|$ and the oscillatory shear index is defined as [68]

$$OSI = \frac{1}{2} \left(1 - \frac{\tau_{mean}}{\tau_{abs}} \right) \quad (14.24)$$

The logarithmic time-averaged WSS distribution is given in Fig. 14.16 along with the OSI distribution. As expected, the peak time-averaged WSS occurs within the ICA in the vicinity of the flow divider. The predicted peak WSS of 805 dyne/cm² is exceptionally high and damaging. Upstream of the stenosis apex lies a band of high time-averaged WSS, across the ICA (400–500 dyne/cm²). This is also greater than the threshold value of 315 dyne/cm² that according to Holme et al. [69] was sufficient to induce platelet activation and enhanced platelet thrombus formation. Immediately downstream of the stenosis lies a small region experiencing time-averaged WSS of

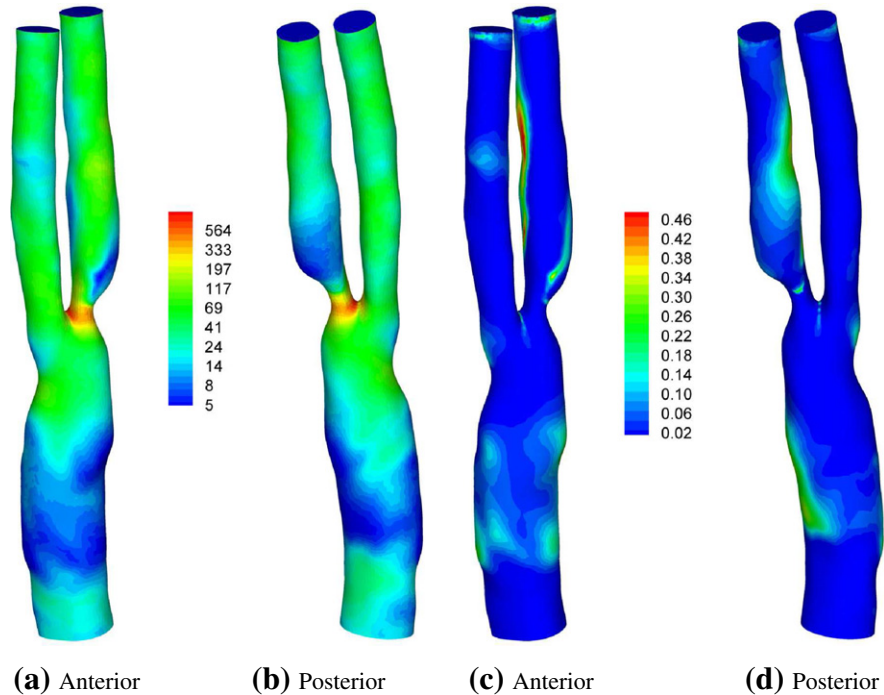


FIGURE 14.16

Hemodynamic wall parameter distributions: (a) and (b) time-averaged WSS [dyne/cm²]; (c) and (d) OSI.

less than 5 dyne/cm² and a bigger region experiencing less than 10 dyne/cm². This region is indicative of a potential location for further plaque formation and it corresponds to the region experiencing flow separation. Away from the stenosis, the majority of the ICA experiences a WSS value less than 40 dyne/cm², although some regions experience values exceeding 100 dyne/cm² along the posterior wall. In the ECA, the time-averaged WSS values range between 20 and 50 dyne/cm². In contrast, approximately 20% of the CCA is predicted to experience a time-averaged WSS of less than 5 dyne/cm² with the vast majority experiencing less than 25 dyne/cm².

The OSI distribution indicates that the regions experiencing low time-averaged WSS in the CCA are coincident with the elevated OSI values. In the ICA, the regions of elevated or high OSI are extensive. A region extends from above the stenosis down the entire length of the inner wall to the ICA outlet. Another region of elevated OSI extends from near the stenosis apex along the outer wall of the ICA. In the ECA, only a small region experiences elevated OSI although this is located distal to the flow divider along the outer wall, which is reminiscent of the regions experiencing low time-averaged WSS in three out of four of the carotids studied by Kaazempur-Mofrad et al. [62]. This region experiences time-averaged WSS of between 5 and 7 dyne/cm².

14.4 Concluding remarks

In this chapter a brief overview on biofluid dynamics modeling within one-dimensional and three-dimensional cardiac frameworks was presented. The vast amount of work done in this area including fluid–structure interaction, mass transport, and other biofluid dynamics problems including human respiratory systems is indicative of the importance of this area. Unfortunately, it is very difficult to cover the entire subject of biofluid dynamics within one chapter. The objective was to provide sufficient information on the fundamentals of two important approaches in biofluid dynamics. We believe we have provided readers with a strong foundation that may be employed in various biofluid dynamics problems.

References

- [1] V.L. Streeter, W.F. Keitzer, D.F. Bohr, Pulsatile pressure and flow through distensible vessels, *Circ. Res.* 13 (1) (1963) 3–20.
- [2] N. Westerhof, F. Bosman, C.J. De Vries, A. Noordergraaf, Analog studies of the human systemic arterial tree, *J. Biomech.* 2 (2) (1969) 121–134.
- [3] B.W. Schaaf, P.H. Abbrecht, Digital computer simulation of human systemic arterial pulse wave transmission: a nonlinear model, *J. Biomech.* 5 (4) (1972) 345–364.

- [4] A.H. Shapiro, Steady flow in collapsible tubes, *J. Biomech. Eng.* 99 (1977) 126–147.
- [5] W. Ruan, M.E. Clark, M. Zhao, A. Curcio, Global solution to a hyperbolic problem arising in the modeling of blood flow in circulatory systems, *J. Math. Anal. Appl.* 331 (2007) 1068–1092.
- [6] A. Avolio, Multi-branched model of the human arterial system, *Med. Biol. Eng. Comput.* 18 (6) (1980) 709–718.
- [7] R. Holenstein, R.M. Nerem, P.F. Niederer, On the propagation of a wave front in viscoelastic arteries, *J. Biomech. Eng.* 106 (2) (1984) 115–122.
- [8] I. Larrabide, P.J. Blanco, S.A. Urquiza, G.R. Feijóo, Sensitivity of blood flow in stenosed carotid bifurcation, in: H. Rodrigues et al. (Eds.), *II International Conference on Computational Bioengineering*, Lisbon, Portugal, 2005.
- [9] J.K. Raines, M.Y. Jaffrin, A.H. Shapiro, A computer simulation of arterial dynamics in the human leg, *J. Biomech.* 7 (1) (1974) 77–91.
- [10] N. Stergiopoulos, D.F. Young, T.R. Rogge, Computer simulation of arterial flow with applications to arterial and aortic stenoses, *J. Biomech.* 25 (12) (1992) 1477–1488.
- [11] S.A. Urquiza, P.J. Blanco, M.J. Vénere, R.A. Feijóo, Multidimensional modelling for the carotid artery blood flow, *Comput. Methods Appl. Mech. Eng.* 195 (33–36) (2006) 4002–4017.
- [12] P.J. Reuderink, H.W. Hoogstraten, P. Sipkema, B. Hillen, N. Westerhof, Linear and nonlinear one-dimensional models of pulse wave transmission at high womersley numbers, *J. Biomech.* 22 (8–9) (1989) 819–827.
- [13] G. Porenta, D.F. Young, T.R. Rogge, A finite-element model of blood flow in arteries including taper, branches, and obstructions, *J. Biomech. Eng.* 108 (2) (1986) 161–167.
- [14] J.P. Mynard, P. Nithiarasu, A 1D arterial blood flow model incorporating ventricular pressure, aortic valve and regional coronary flow using the locally conservative Galerkin (LCG) method, *Commun. Numer. Methods Eng.* 24 (2008) 367–417.
- [15] P. Reymond, F. Merenda, F. Perren, D. Rufenacht, N. Stergiopoulos, Validation of a one-dimensional model of the systemic arterial tree, *Am. J. Phys. Heart Circ. Phys.* 297 (2009) H208–H222.
- [16] F.Y. Liang, S. Takagi, R. Himeno, H. Liu, Multi-scale modeling of the human cardiovascular system with applications to aortic valvular and arterial stenoses, *Med. Biol. Eng. Comput.* 47 (2009) 743–755.
- [17] F.Y. Liang, S. Takagi, R. Himeno, H. Liu, Biomechanical characterization of ventricular-arterial coupling during aging: a multi-scale model, study, *J. Biomech.* 42 (2009) 692–704.
- [18] J.J. Wang, K.H. Parker, Wave propagation in a model of the arterial circulation, *J. Biomech.* 37 (2004) 457–470.
- [19] R.M. Berne, M.N. Levy, *Cardiovascular Physiology*, The Mosby Physiology Monograph Series, eighth ed., Mosby, Inc., Missouri, USA, 2001.

- [20] J.J. Wang, K.H. Parker, Wave propagation in a model of the arterial circulation, *J. Biomech.* 37 (4) (2004) 457–470.
- [21] J.A. Rumberger, R.M. Nerem, A method-of-characteristics calculation of coronary blood flow, *J. Fluid Mech.* 82 (3) (1977) 429–448.
- [22] C. Guiot, G. Pianta, C. Cancelli, T.J. Pedley, Prediction of coronary blood flow with a numerical model based on collapsible tube dynamics, *Am. J. Phys.* 258 (1990) H1606–H1614.
- [23] B.S. Gow, C.D. Hadfield, The elasticity of canine and human coronary arteries with reference to postmortem changes, *Circ. Res.* 45 (5) (1979) 588–594.
- [24] C. Cuspidi, L. Lonati, L. Sampieri, L. Valagussa, I. Michev, G. Leonetti, A. Zanchetti, Lack of correlation between left ventricular mass and diameter of left coronary artery main trunk in hypertensive patients, *Am. J. Hypertens.* 12 (12) (1999) 1163–1168.
- [25] A. Ranga, O. Bouchot, R. Mongrain, P. Ugolini, R. Cartier, Computational simulations of the aortic valve validated by imaging data: evaluation of valve-sparing techniques, *Inter. Cardiovasc. Thorac. Surg.* 5 (4) (2006) 373–378.
- [26] D.J. Brown, Input impedance and reflection coefficient in fractal-like models of asymmetrically branching compliant tubes, *IEEE Trans. Biomed. Eng.* 43 (7) (1996) 715–722.
- [27] R.W. Glenny, H.T. Robertson, Fractal properties of pulmonary blood flow: characterization of spatial heterogeneity, *J. Appl. Phys.* 69 (2) (1990) 532–545.
- [28] G.S. Krenz, J.H. Linehan, C.A. Dawson, A fractal continuum model of the pulmonary arterial tree, *J. Appl. Phys.* 72 (6) (1992) 2225–2237.
- [29] S.J. Sherwin, L. Formaggia, J. Peiró, V. Franke, Computational modelling of 1D blood flow with variable mechanical properties and its application to the simulation of wave propagation in the human arterial system, *Int. J. Numer. Methods Fluids* 43 (6–7) (2003) 673–700.
- [30] C. Sheng, S. Sarwal, K. Watts, A. Marble, Computational simulation of blood flow in human systemic circulation incorporating an external force field, *Med. Biol. Eng. Comput.* 33 (1) (1995) 8–17.
- [31] G.H. Golub, C.F. Van Loan, *Matrix Computations*, John Hopkins University Press, Baltimore, 1996.
- [32] J. Wan, B. Steele, S.A. Spicer, S. Strohband, G.R. Feijóo, T.J.R. Hughes, C.A. Taylor, A one-dimensional finite element method for simulation-based medical planning for cardiovascular disease, *Comput. Methods Biomech. Biomed. Eng.* 5 (3) (2002) 195–206.
- [33] M.S. Olufsen, Structured tree outflow condition for blood flow in larger systemic arteries, *Am. J. Phys.* 276 (1) (1999) H257–H268.
- [34] M. Anliker, R.L. Rockwell, E. Ogden, Nonlinear analysis of flow pulses and shock waves in arteries, part I: derivation and properties of mathematical model, *Z. Angew. Math. Phys.* 22 (2) (1971) 217–246.
- [35] S. Einav, S. Aharoni, M. Manoach, Exponentially tapered transmission line model of the arterial system, *IEEE Trans. Biomed. Eng.* 35 (5) (1988) 333–339.

- [36] K.-C. Chang, T.-S. Kuo, Exponentially tapered T-tube model in the characterization of arterial non-uniformity, *J. Theor. Biol.* 183 (1) (1996) 35–46.
- [37] R. Fogliardi, R. Burattini, K.B. Campbell, Identification and physiological relevance of an exponentially tapered tube model of canine descending aortic circulation, *Med. Eng. Phys.* 19 (3) (1997) 201–211.
- [38] L.J. Myers, W.L. Capper, Exponential taper in arteries: an exact solution of its effect on blood flow velocity waveforms and impedance, *Med. Eng. Phys.* 26 (2) (2004) 147–155.
- [39] M. Anliker, M.B. Hstand, E. Ogden, Dispersion and attenuation of small artificial pressure waves in the canine aorta, *Circ. Res.* 23 (4) (1968) 539–551.
- [40] M.P. Spencer, F.C. Greiss, Dynamics of ventricular ejection, *Circ. Res.* 10 (1962) 274–279.
- [41] M.I. Noble, The contribution of blood momentum to left ventricular ejection in the dog, *Circ. Res.* 23 (5) (1968) 663–670.
- [42] R. Kelly, C. Hayward, A. Avolio, M. O'Rourke, Noninvasive determination of age-related changes in the human arterial pulse, *Circulation* 80 (6) (1989) 1652–1659.
- [43] W.M. Chilian, M.L. Marcus, Phasic coronary blood flow velocity in intramural and epicardial coronary arteries, *Circ. Res.* 50 (6) (1982) 775–781.
- [44] T. Matsumoto, F. Kajiya, Coronary microcirculation: physiology and mechanics, *Fluid Dynam. Res.* 37 (2005) 60–81.
- [45] E. Toyota, Y. Ogasawara, O. Hiramatsu, H. Tachibana, F. Kajiya, S. Yamamori, W.M. Chilian, Dynamics of flow velocities in endocardial and epicardial coronary arterioles, *Am. J. Phys.* 288 (4) (2005) H1598–H1603.
- [46] H.S. Lowensohn, E.M. Khouri, D.E. Gregg, R.L. Pyle, R.E. Patterson, Phasic right coronary artery blood flow in conscious dogs with normal and elevated right ventricular pressures, *Circ. Res.* 39 (6) (1976) 760–766.
- [47] E.M. Khouri, D.E. Gregg, C.R. Rayford, Effect of exercise on cardiac output, left coronary flow and myocardial metabolism in the unanesthetized dog, *Circ. Res.* 17 (5) (1965) 427–437.
- [48] L.A. Nikolaidis, A. Doverspike, R. Huerbin, T. Hentosz, R.P. Shannon, Angiotensin-converting enzyme inhibitors improve coronary flow reserve in dilated cardiomyopathy by a bradykinin-mediated, nitric oxide-dependent mechanism, *Circulation* 105 (23) (2002) 2785–2790.
- [49] D.M. Griggs, C.C. Chen, Coronary hemodynamics and regional myocardial metabolism in experimental aortic insufficiency, *J. Clin. Invest.* 53 (1974) 1599–1606.
- [50] A. Kenny, C.R. Wisbey, L.M. Shapiro, Profiles of coronary blood flow velocity in patients with aortic stenosis and the effect of valve replacement: a transthoracic echocardiographic study, *Br. Heart J.* 71 (1994) 57–62.
- [51] H.N. Sabbah, P.D. Stein, Effect of aortic stenosis on coronary flow dynamics: studies in an in-vitro pulse duplicating system, *J. Biomech. Eng.* 104 (1982) 221–225.

- [52] S.Y. Yeo, X. Xie, I. Sazonov, P. Nithiarasu, Geometric potential force for the deformable model, in: British Machine Vision Conference, 2009.
- [53] S.Y. Yeo, X. Xie, I. Sazonov, P. Nithiarasu, Geometrically induced force interaction for three-dimensional deformable models, in: IEEE Transactions of Image Processing, 2010.
- [54] X. Xie, M. Mirmehdi, MAC: magnetostatic active contour model, IEEE Trans. Pattern Anal. Mach. Intell. 30 (4) (2008) 632–647.
- [55] P.F. Felzenszwalb, D.P. Huttenlocher. Distance transforms of sampled functions, Cornell Computing and Information Science, TR2004-1963, 2004.
- [56] J.A. Sethian, Level Set Methods and Fast Marching Methods: Evolving Interfaces in Computational Geometry, Fluid Mechanics, Computer Vision, and Material Science, Cambridge University Press, Cambridge, UK, 1999.
- [57] I. Sazonov, S.Y. Yeo, R.L.T. Bevan, X. Xie, R. van Loon, P. Nithiarasu, Modelling pipeline for subject-specific arterial blood flow – a review, Int. J. Numer. Methods Biomed. Eng. 27 (2011) 1868–1910.
- [58] O. Smedby, Do plaques grow upstream or downstream? An angiographic study in the femoral artery, Arterioscl. Throm. Vasc. Biol. 17 (1997) 912–918.
- [59] D.N. Ku, D.P. Giddens, C.K. Zarins, S. Glagov, Pulsatile flow and atherosclerosis in the human carotid bifurcation – positive correlation between plaque location and low and oscillating shear-stress, Atherosclerosis 5 (3) (1985) 293–302.
- [60] F.P. Glor, Q. Long, A.D. Hughes, A.D. Augst, B. Ariff, S.A. McG, Thom P.R. Verdonck, X.Y. Xu, Reproducibility study of magnetic resonance image-based computational fluid dynamics prediction of carotid bifurcation flow, Ann. Biomed. Eng. 31 (2003) 142–151.
- [61] P. Papathanasopoulou, S. Zhao, U. Köhler, M.B. Robertson, Q. Long, P. Hoskins, MRI measurement of time-resolved wall shear stress vectors in a carotid bifurcation model, and comparison with CFD predictions, J. Magn. Reson. Imag. 17 (2003) 153–162.
- [62] M.R. Kaazempur Mofrad, A.G. Isasi, H.F. Younis, R.C. Chan, D.P. Hinton, G. Sukhova, G.M. LaMuraglia, R.T. Lee, R.D. Kamm, Characterization of the atherosclerotic carotid bifurcation using MRI finite element modeling, and histology, Ann. Biomed. Eng. 32 (2004) 932–946.
- [63] S.A. Urquiza, P.J. Blanco, M.J. Vénere, R.A. Feijóo, Multidimensional modelling for the carotid artery blood flow, Comput. Methods Appl. Mech. Eng. 195 (2006) 4002–4017.
- [64] A.D. Jeays, P.V. Lawford, R. Gillott, P. Spencer, D.C. Barber, K.D. Bardhan, D.R. Hose, Characterisation of the haemodynamics of the superior mesenteric artery, J. Biomech. 40 (2007) 1916–1926.
- [65] K.E. Lee, K.H. Parker, C.G. Caro, S.J. Sherwin, The spectral/hp element modelling of steady flow in non-planar double bends, Int. J. Numer. Methods Fluids 57 (2008) 519–529.

- [66] K.T. Nguyen, C.D. Clark, T.J. Chancellor, D.V. Papavassiliou, Carotid geometry effects on blood flow and on risk for vascular disease, *J. Biomech.* 41 (2008) 11–19.
- [67] A.M. Malek, S.L. Alper, S. Izumo, Hemodynamic shear stress and its role in atherosclerosis, *JAMA* 282 (1999) 2035–2042.
- [68] X. He, D.N. Ku, Pulsatile flow in the human left coronary artery bifurcation: average conditions, *J. Biomech. Eng.* 118 (1996) 74–82.
- [69] P.A. Holme, U. Orvim, M.J.A.G. Hamers, N.O. Solum, F.R. Brosstad, R.M. Barstad, K.S. Sakariassen, Shear-induced platelet activation and platelet microparticle formation at blood flow conditions as in arteries with a severe stenosis, *Arterioscl. Throm. Vasc. Biol.* 17 (1997) 646–653.